

Co₃O₄/g-C₃N₄ Hybrids for Gas-Phase Hg⁰ Removal at Low Temperature

Authors:

Zhen Zhang, Jiang Wu, Dongjing Liu

Date Submitted: 2019-07-30

Keywords: elemental mercury, cobalt oxide, carbon nitride nanosheet, mercury removal

Abstract:

The Co₃O₄/g-C₃N₄ hybrids are constructed via the incipient wetness impregnation method by depositing Co₃O₄ onto the exterior of g-C₃N₄, and then employed for Hg⁰ capture within 60–240 °C. The results show that the Co₃O₄/g-C₃N₄ hybrid with a Co₃O₄ content of 12 wt% performs optimally with the highest Hg⁰ removal efficiency of ~100% at or above 120 °C. The high performances of the Co₃O₄/g-C₃N₄ hybrids are probably attributed to the tight interfacial contact between Co₃O₄ and g-C₃N₄, with its improved electron transfer, inferring that cobalt oxide and g-C₃N₄ display a cooperative effect towards Hg⁰ removal. NO and SO₂ shows a significant suppressive influence on the mercury capture performance, plausibly owing to the competing adsorption and side reactions.

Record Type: Published Article

Submitted To: LAPSE (Living Archive for Process Systems Engineering)

Citation (overall record, always the latest version):

LAPSE:2019.0850

Citation (this specific file, latest version):

LAPSE:2019.0850-1

Citation (this specific file, this version):


LAPSE:2019.0850-1v1

DOI of Published Version: <https://doi.org/10.3390/pr7050279>

License: Creative Commons Attribution 4.0 International (CC BY 4.0)

Article

Co₃O₄/g-C₃N₄ Hybrids for Gas-Phase Hg⁰ Removal at Low Temperature

Zhen Zhang ¹, Jiang Wu ^{1,*} and Dongjing Liu ^{2,*} 

¹ College of Energy and Mechanical Engineering, Shanghai University of Electric Power, Shanghai 200090, China; zhangzhensuep@163.com

² School of Energy and Power Engineering, Jiangsu University, Zhenjiang 212013, China

* Correspondence: wujiang207@163.com (J.W.); liudongjing19@163.com or liudongjing@ujs.edu.cn (D.L.); Tel./Fax: +86-021-3530-3902 (J.W.); +86-0511-8878-0211 (D.L.)

Received: 1 April 2019; Accepted: 6 May 2019; Published: 13 May 2019



Abstract: The Co₃O₄/g-C₃N₄ hybrids are constructed via the incipient wetness impregnation method by depositing Co₃O₄ onto the exterior of g-C₃N₄, and then employed for Hg⁰ capture within 60–240 °C. The results show that the Co₃O₄/g-C₃N₄ hybrid with a Co₃O₄ content of 12 wt% performs optimally with the highest Hg⁰ removal efficiency of ~100% at or above 120 °C. The high performances of the Co₃O₄/g-C₃N₄ hybrids are probably attributed to the tight interfacial contact between Co₃O₄ and g-C₃N₄, with its improved electron transfer, inferring that cobalt oxide and g-C₃N₄ display a cooperative effect towards Hg⁰ removal. NO and SO₂ shows a significant suppressive influence on the mercury capture performance, plausibly owing to the competing adsorption and side reactions.

Keywords: mercury removal; carbon nitride nanosheet; cobalt oxide; elemental mercury

1. Introduction

Mercury, as a kind of heavy metal, is a persistent toxic substance of increasing concern worldwide [1,2]. The combustion of coal accounts for the great majority of the global anthropogenic mercury emissions [3]. Coal-fired mercury can be empirically classified into three main forms: elemental mercury (Hg⁰), oxidized mercury (Hg²⁺), and particulate mercury (Hg(p)). Hg²⁺ and Hg(p) can be removed using wet scrubbers and fabric filters, respectively [4]. However, elemental mercury (Hg⁰), the predominant speciation of coal-derived mercury, is hardly captured by the available pollutant control facilities because it is highly volatile, chemically stable, and water insoluble [5]. Catalytic oxidation and adsorption is considered to be the most effective and viable method for the reduction of Hg⁰ emission [6]. Activated carbon is frequently used for mercury emission control in power plants [7]. Nevertheless, the high operation cost, low mercury capacity, and negative effect on fly ash quality has restrained its widespread application in coal-fired power plants [8]. Currently, transition-metal oxides, such as CuO [9], MnO₂ [10], Fe₂O₃ [11], and Co₃O₄ [12], have been recognized as potential sorbents or catalysts for Hg⁰ removal because of their excellent redox abilities and lower capital cost. CeO₂, as a rare-earth oxide, has also been employed as an additive, active ingredient, and carrier in the synthesis of composites for mercury capture, attributed to the CeO₂/Ce₂O₃ redox couple and structure defect [13].

Metal oxides loading onto the exterior of nano-materials is a type of catalyst with good adsorption as well as redox ability [14]. Thus, these catalysts could be potential candidates for capturing Hg⁰ from coal combustion flue gas. Graphite-like carbon nitride (g-C₃N₄), the most stable allotrope of versatile CN structures, has been widely studied in many scientific fields because of its distinct electronic structure, thermal stability, ample source as well as simple synthesis route [15]. Two-dimensional g-C₃N₄ nanosheet possesses the advantage of providing more anchoring sites for bare metal oxide

loading [16]. Besides, the metal oxide/g-C₃N₄ composites and their intimate interfacial contact, with reduced potential energy barrier and improved charge transfer mobility, are expected to facilitate Hg⁰ oxidation [17,18]. The Nb₂O₅/g-C₃N₄ hybrids outperformed the individual Nb₂O₅ and g-C₃N₄ in photocatalytic reactions due to the sufficient interfacial interaction of Nb₂O₅ and g-C₃N₄ through a direct Z-scheme [19]. Co₃O₄ embedded into tubular nanostructures of the g-C₃N₄ lead to prominent performances for oxygen and hydrogen evolution reactions [20]. Mesoporous Co₃O₄ anchored onto g-C₃N₄ would greatly promote the composite conductivity and boost the charge transfer mobility, thereby enhancing the performance of capacitance [21].

Despite the immense applications of the metal oxide/g-C₃N₄ hybrids, Co₃O₄/g-C₃N₄ hybrids so far have not been explored for mercury capture from coal-derived flue gas. In this work, Co₃O₄/g-C₃N₄ hybrids are facilely constructed by tuning the content of Co₃O₄ deposited on g-C₃N₄ exterior via an incipient wetness impregnation approach and then applied for gas-phase Hg⁰ removal in an upflow packed-bed quartz type reactor in a temperature range of 60–240 °C. The Co₃O₄/g-C₃N₄ hybrids are examined by using field emission scanning electron microscopy (FESEM), transmission electron microscopy (TEM), X-ray diffraction (XRD), nitrogen adsorption-desorption, Fourier transform infrared spectroscopy (FTIR), and X-ray photoelectron spectroscopy (XPS) techniques. The effects of the Co₃O₄ loading values, reaction temperature, and flue gas component on the mercury capture performances of the Co₃O₄/g-C₃N₄ hybrids are studied. The mechanism of Hg⁰ oxidation over Co₃O₄/g-C₃N₄ hybrids is discussed therewith.

2. Experimental Section

2.1. Preparation of Co₃O₄/g-C₃N₄ Hybrids

The g-C₃N₄ nanosheets (CNNS) were synthesized via a two-step calcination approach as reported in [22,23]. The Co₃O₄/g-C₃N₄ hybrids were synthesized using an incipient wetness method. Versatile amounts of Co(NO₃)₂·6H₂O were dissolved in ultrapure water and mixed with CNNS in a beaker which was then dried at 343 K overnight. Eventually, the formed solids were calcined at 473 K for 2 h [23]. The final specimens are denoted as *x*Co₃O₄/CNNS, with *x* representing the weight content (wt%) of Co₃O₄ in the hybrids.

2.2. Characterization of Co₃O₄/g-C₃N₄ Hybrids

The FESEM images were attained on a Phillips XL-30 FEG/NEW instrument (Eindhoven, The Netherlands). The TEM images were acquired on a Phillips Model CM200 device (Amsterdam, The Netherlands). The XRD patterns were measured on Bruker D8 Advance equipment (Karlsruhe, Germany). The nitrogen isotherms were examined on a Beishide 3H-2000PS4 apparatus (Beijing, China). The FTIR profiles were determined on a FTIR-8400S spectrometer (Shimadzu Corporation, Kyoto, Japan). The XPS analysis were performed on a RBD-upgraded PHI-5000C ESCA system (Perkin Elmer, Waltham, MA, USA) [24].

2.3. Mercury Oxidation

The mercury removal experimental system has been fully expressed in previous papers [23,25]. As depicted in Figure 1, 50 mg of specimens were put into the middle of the reactor and fixed with quartz wool at the tail of the sorbent bed. After heating to the desired temperatures, the Hg⁰-laden stream, originating from a PSA device (PS Analytical, Kent, UK), was then consecutively charged into the reactor for mercury oxidation tests. The influent and effluent mercury concentration was examined by an online mercury analyzer (Lumex, RA-915-M, St. Petersburg, Russia). Moreover, active carbon was used for the off-gas cleaning. It can adsorb the oxidized mercury as well as elemental mercury in the flue gas.

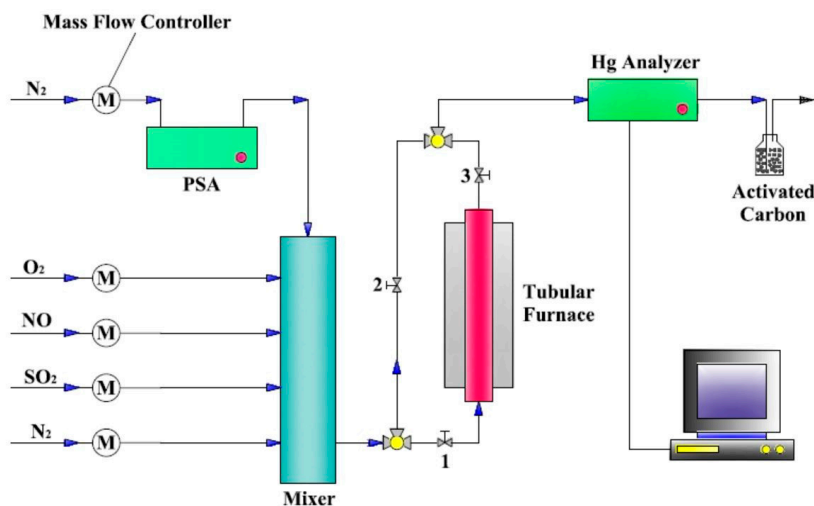


Figure 1. Schematic drawing of mercury removal experimental system.

3. Results and discussion

3.1. Characterization Analysis

The FESEM image and photo of the CNNS are shown in Figure 2. CNNS displays a light-yellow color (the inset in Figure 2a) and it consists of many lamellar structures with lateral sizes of $<1\ \mu\text{m}$ (Figure 2a) and thickness of dozens of nanometers (Figure 2b). The CNNS displays transparent characteristics, indicating the super-thin sheet-like morphology of the CNNS with $\sim 1\text{--}10\ \text{nm}$ in thickness and $\sim 1\text{--}3\ \mu\text{m}$ in size (Figure 3a). The TEM image and the selected area electron diffraction (SAED) analysis of the $12\text{Co}_3\text{O}_4/\text{CNNS}$ are displayed in Figure 3b. The lattice fringes of Co_3O_4 are closely surrounded by $g\text{-C}_3\text{N}_4$. The intimate interfacial contact implies the good interaction between Co_3O_4 and $g\text{-C}_3\text{N}_4$, which is beneficial for electron transfer and, thus, promoting Hg^0 oxidation [26]. The diffraction spots with a distance of 0.205 and 0.429 nm are ascribed to the reflection of the Co_3O_4 (400) and Co_3O_4 (111) lattice plane, respectively. The XRD spectra of the pure and Co_3O_4 -modified CNNS are displayed in Figure 4. The intense peaks at $\sim 27.7^\circ$ detected in all specimens belong to the reflection of the (002) crystal face of $g\text{-C}_3\text{N}_4$ (JCPDS no. 87-1526) [27]. The signals at 31.1° , 36.7° , 44.8° , 59.4° , and 65.1° are assigned to the diffraction of Co_3O_4 (JCPDS no. 42-1467) [28]. With the increment of the Co_3O_4 content, its feature peaks gradually increase in intensity, suggesting that Co_3O_4 has been successfully deposited on $g\text{-C}_3\text{N}_4$ surface.

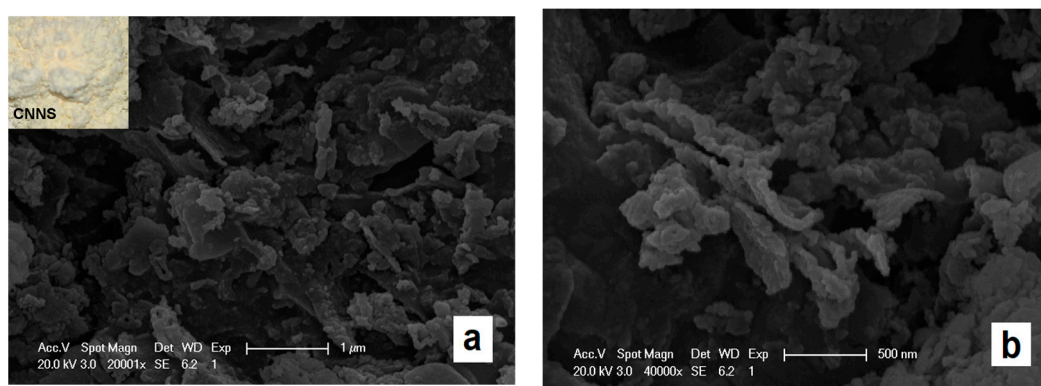


Figure 2. FESEM image and photo of $g\text{-C}_3\text{N}_4$ nanosheets (CNNS).

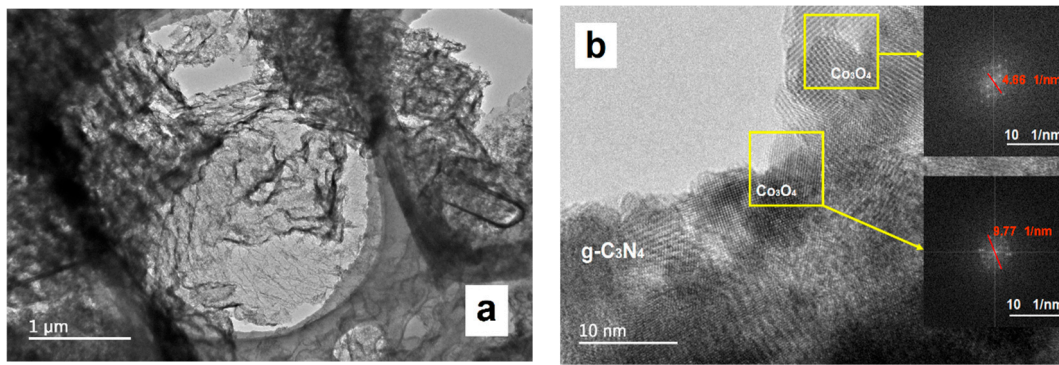


Figure 3. (a) TEM image of CNNS and (b) TEM image and selected area electron diffraction (SAED) analysis of $12\text{Co}_3\text{O}_4/\text{CNNS}$.

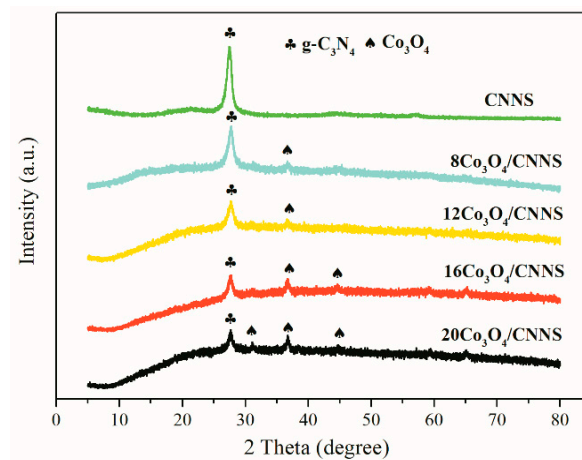


Figure 4. XRD patterns of pure and Co_3O_4 -modified CNNS.

The nitrogen isotherms of the pure and Co_3O_4 -modified CNNS are presented in Figure 5. Hysteresis loops were observed in all specimens at higher relative pressure. The nitrogen uptakes at lower relative pressures were fairly less, implying that enormous mesoporous structures presented on the catalyst surface [29]. The pure CNNS had a large BET surface area of $109 \text{ m}^2/\text{g}$ and large average pore size of 19 nm (Table 1). After incorporating Co_3O_4 , they all reduced significantly. The BET surface area and average pore size of $x\text{Co}_3\text{O}_4/\text{CNNS}$ dropped to $27\text{--}42 \text{ m}^2/\text{g}$ and $10\text{--}12 \text{ nm}$, respectively. The probable reason for this is that parts of the mesoporous structures of the CNNS were filled or blocked by Co_3O_4 grains [30].

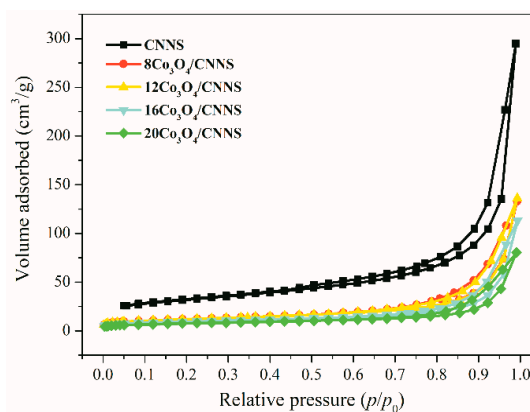
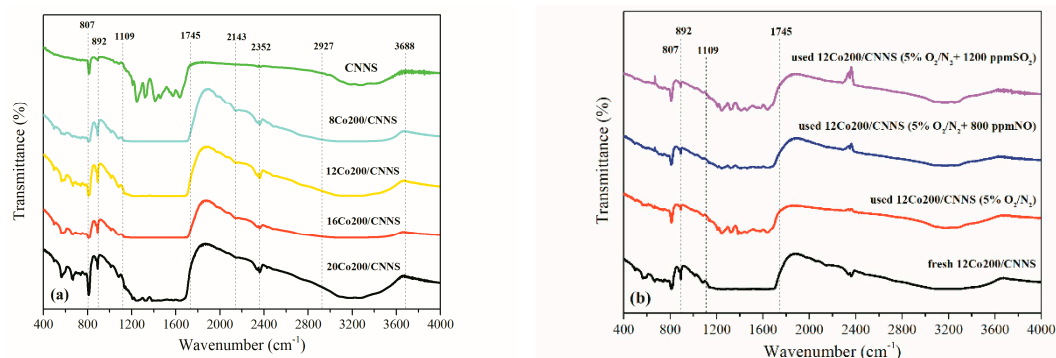


Figure 5. Nitrogen isotherms of pure and Co_3O_4 -modified CNNS.

Table 1. Textural property and average pore diameter of the pure and Co₃O₄-modified CNNS.

Samples	BET Surface Area (m ² /g)	Total Pore Volume (cm ³ /g)	Micropore Volume (cm ³ /g)	Mesopore Volume (cm ³ /g)	Pore Diameter (nm)
CNNS	109	0.456	0.011	0.445	19
8Co ₃ O ₄ /CNNS	42	0.206	0.004	0.202	10
12Co ₃ O ₄ /CNNS	42	0.211	0.003	0.208	11
16Co ₃ O ₄ /CNNS	33	0.175	0.003	0.172	12
20Co ₃ O ₄ /CNNS	27	0.125	0.002	0.123	10

The FTIR profiles of fresh CNNS and $x\text{Co}_3\text{O}_4/\text{CNNS}$ are displayed in Figure 6a. The two sharp signals at ~ 892 and $\sim 807\text{ cm}^{-1}$ are in accord with the feature breathing pattern of the triazine loop units stemming from polymerized C–N heterocycles [31]. The set of peaks between ~ 1109 and $\sim 1745\text{ cm}^{-1}$ belong to the aromatic C–N stretch oscillation [32]; the weak bands at $\sim 2143\text{ cm}^{-1}$ correspond to the cyano C \equiv N terminal groups [33]. The peaks at $\sim 2352\text{ cm}^{-1}$ belong to the O=C=O asymmetrical stretch oscillation of the carbon dioxide adhered to the catalyst exterior [34]. The broad bands between 2927 and 3688 cm^{-1} relate to the N–H stretch oscillation of unpolymerized $-\text{NH}_2$ functions and the O–H stretch oscillation of the H₂O molecules adhered to the catalyst exterior [35]. As depicted in Figure 6b, the main feature peaks of the g-C₃N₄ can be distinctly detected in the spent 12Co₃O₄/CNNS, indicating that the atomic structures of the 12Co₃O₄/CNNS retain the same during Hg⁰ removal reactions.

**Figure 6.** FTIR profiles: (a) fresh CNNS and $x\text{Co}_3\text{O}_4/\text{CNNS}$; (b) fresh and spent 12Co₃O₄/CNNS.

The surface elemental valences of 12Co₃O₄/CNNS before and after reaction were examined by XPS, as presented in Figure 7. The bands at ~ 284.6 and $\sim 285.2\text{ eV}$ relate to the sp^2 -bonded carbon atoms, while the peaks at ~ 287.6 and $\sim 288.2\text{ eV}$ are associated with the N–C=N structures [36]. The peaks at ~ 398.0 and $\sim 398.4\text{ eV}$ belong to the hybridized secondary nitrogen (C–N=C). The bands at ~ 399.0 and $\sim 399.2\text{ eV}$ are related to the hybridized tertiary nitrogen (N–(C)₃). The peaks at ~ 400.0 and $\sim 400.4\text{ eV}$ correspond to the $-\text{NH}_2$ groups [37]. What is more, the C 1s and N 1s binding energies of the used 12Co₃O₄/CNNS are smaller than those of the fresh one. This suggests that Hg⁰ probably donates electrons to g-C₃N₄ during mercury removal reactions. With respect to the Co 2p spectrum, the bands at ~ 782.0 and $\sim 782.8\text{ eV}$ are supposed to be the reflection of the Co³⁺ in the Co₃O₄, while the peaks at ~ 786.4 and $\sim 787.4\text{ eV}$ relate to the signals of the Co²⁺ in the Co₃O₄ [38]. The ratio of Co³⁺/Co²⁺ for the fresh specimen is ~ 0.83 . It slightly decreases to ~ 0.75 for the spent specimen. This indicates that a fraction of the Co³⁺ cations transferred into the Co²⁺ cations after Hg⁰ oxidation. The Co³⁺ cations are involved in the mercury oxidation reactions. The bands at $\sim 531.8\text{ eV}$ belong to the chemisorbed oxygen (O_α) on the catalyst exterior, while the peaks at $\sim 533.2\text{ eV}$ are linked to the oxygen (O_β) in the $-\text{OH}$ group or C–O bond [39]. The percentage of the chemisorbed oxygen increased from ~ 54.7 to $\sim 61.3\%$ for the 12Co₃O₄/CNNS before and after the reaction, correspondingly, which infers that the gaseous O₂ from the feed gas may replenish the depleted chemisorbed oxygen during the Hg⁰ oxidation processes. The Hg 4f spectra displays two feature peaks at ~ 101.4 and $\sim 103.6\text{ eV}$, which

implies the generation of HgO [40]. Moreover, the absence of the feature peak of elemental mercury at 99.9 eV indicates that Hg⁰ adsorption over 12Co₃O₄/CNNS is governed by chemisorptions [41].

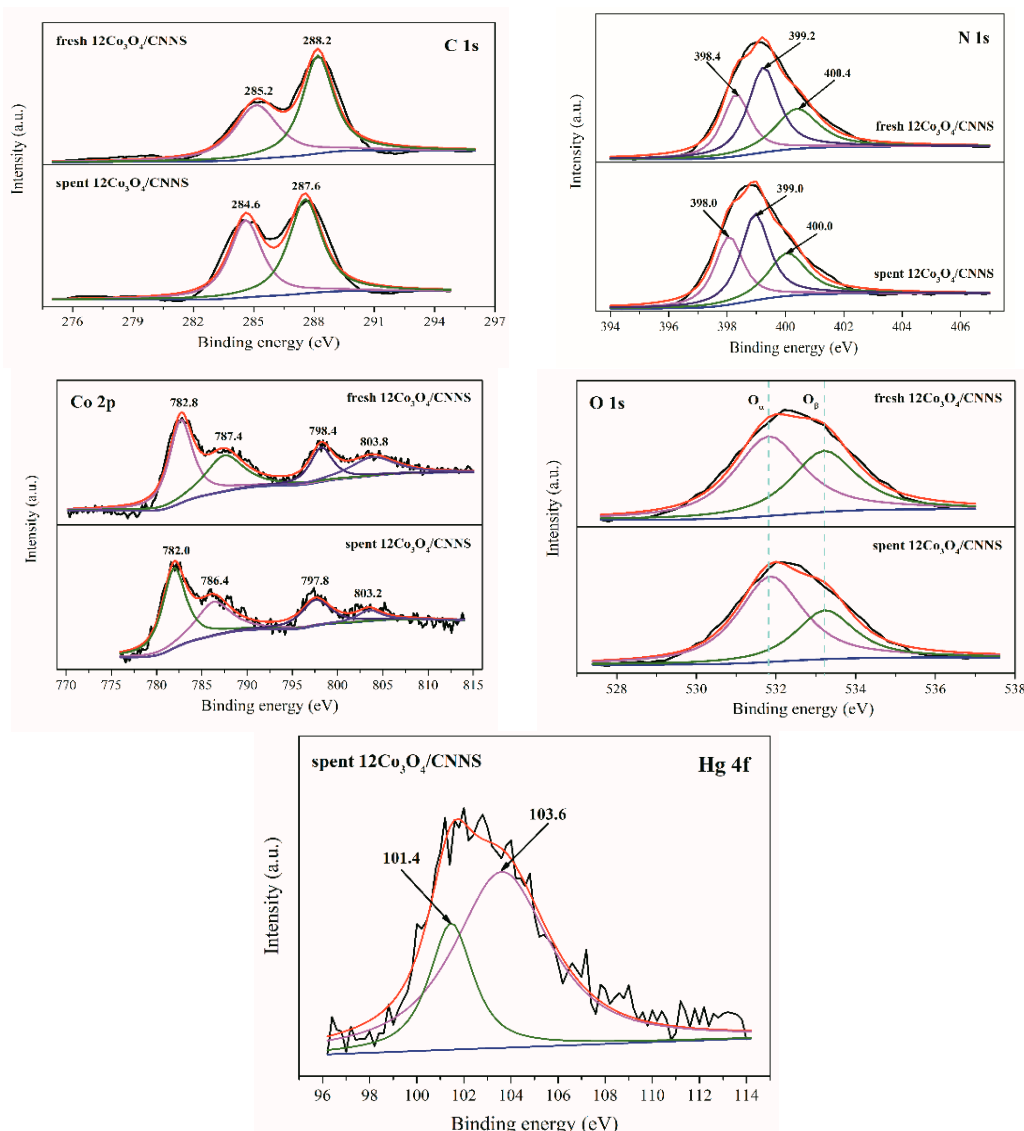


Figure 7. XPS spectra of 12Co₃O₄/CNNS before and after the reaction.

3.2. Impact of Loading Value

The performances of the pure and Co₃O₄-modified CNNS with respect to elemental mercury removal at 120 °C in 5% O₂/N₂ over 90 min are presented in Figure 8. The pristine CNNS shows good Hg⁰ capture ability, plausibly because of the distinct C–N structure and considerable surface area. The equilibrium Hg⁰ removal efficiency is ~59.0%. Incorporating Co₃O₄ with g-C₃N₄ could remarkably enhance the Hg⁰ removal ability. The Hg⁰ sorption rate at the initial stage and the Hg⁰ removal efficiency both increase after the addition of Co₃O₄. The mercury conversion rises from ~59.0 to ~86.0% as the Co₃O₄ loading value elevates from 0 to 8 wt%. The 12Co₃O₄/CNNS performs the best with mercury conversion reaching ~100%, indicating that the Co₃O₄ modification contributes to Hg⁰ removal by the introduction of added reactive sites. Moreover, the tight interfacial interaction of Co₃O₄ and g-C₃N₄, with promoted charge transfer mobility, can facilitate redox reactions, which could enhance mercury conversion. Nevertheless, the redox ability would decline with further incremental Co₃O₄ content. The mercury conversion subtly drops to ~97.5% when loading value exceeds 12 wt%, presumably owing to the significant reduction of the surface area. Thus, the best Co₃O₄ content for

$x\text{Co}_3\text{O}_4/\text{CNNS}$ is 12 wt%. What is more, bare Co_3O_4 exhibits a poor performance towards mercury adsorption with a mercury conversion of only $\sim 36.3\%$, probably owing to its larger grain size and lower surface area. Thus, it can be concluded that Co_3O_4 and $g\text{-C}_3\text{N}_4$ display a cooperative effect towards Hg^0 removal.

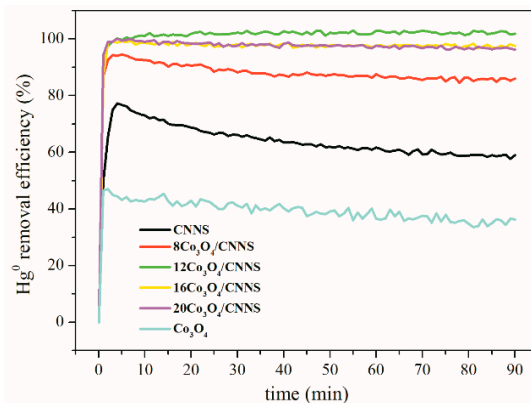


Figure 8. The Hg^0 capture performances of pure and Co_3O_4 -modified CNNS.

3.3. Impact of Reaction Temperature

The mercury conversion of the $12\text{Co}_3\text{O}_4/\text{CNNS}$ at $60\text{--}240\text{ }^\circ\text{C}$ in $5\% \text{O}_2/\text{N}_2$ is presented in Figure 9. It is found that temperature could significantly affect mercury removal performance. Fairly low mercury oxidation activity was exhibited at $60\text{ }^\circ\text{C}$ by $12\text{Co}_3\text{O}_4/\text{CNNS}$, with a mercury conversion of only $\sim 33.3\%$. The performance of mercury oxidation can be remarkably enhanced when temperature goes up to $90\text{ }^\circ\text{C}$, with mercury conversion swiftly rising to $\sim 98.4\%$. A mercury conversion of 100% can be reached at temperature above or at $120\text{ }^\circ\text{C}$. The lower reaction activity is attributed to the lower reaction rate at lower temperatures, while higher temperature facilitates chemisorption processes because of the decreased activation energy barrier. As displayed in Figure 10, CNNS shows an unstable performance, with mercury conversion gradually dropping from ~ 77.2 to $\sim 47.3\%$ as time passed likely attributed to the consumption of the active sorption sites. In contrast, $12\text{Co}_3\text{O}_4/\text{CNNS}$ performs stably, with mercury conversion rapidly reaching $\sim 100\%$ within ~ 42 min and then leveling off as time passes, plausibly owing to its prominent redox ability.

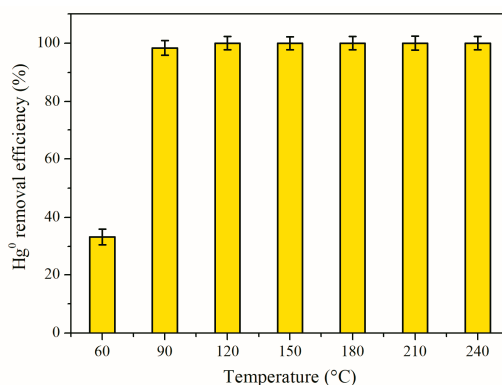


Figure 9. Impact of reaction temperature on the mercury conversion of $12\text{Co}_3\text{O}_4/\text{CNNS}$.

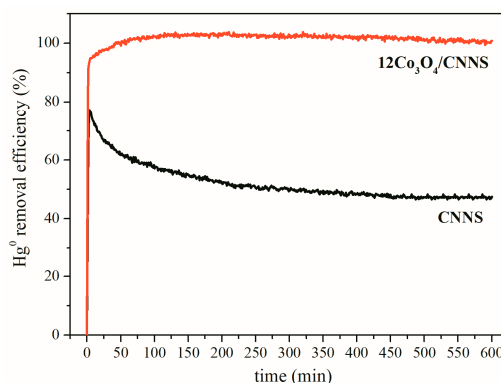


Figure 10. The performances of CNNS and 12Co₃O₄/CNNS towards elemental mercury removal at 120 °C over 600 min on 5% O₂/N₂ stream.

3.4. Impact of Flue Gas

Nitrogen monoxide and sulfur dioxide are the predominant acidic gas components in coal-derived flue gas. The influences of NO and SO₂ on the mercury conversion of 12Co₃O₄/CNNS at 120 °C is shown in Figure 11. It is found that NO and SO₂ both show detrimental impacts on Hg⁰ removal processes. The mercury conversion of 12Co₃O₄/CNNS was significantly reduced to ~44.6 and ~42.7% after adding 800 ppm NO and 1200 ppm SO₂ into the feed gas, respectively. This suggests that NO or SO₂ molecules and Hg⁰ vapor could be competitively adsorbed on the surface of 12Co₃O₄/CNNS [9]. In addition, the adsorbed SO₂ may react with Co₃O₄ to produce thermally-stable metal sulfates, i.e., cobalt sulfate, leading to the decline of the active phases [42]. Thus, the competitive adsorption and side reactions contribute to the remarkable suppressive influences of NO and SO₂ towards Hg⁰ adsorption.

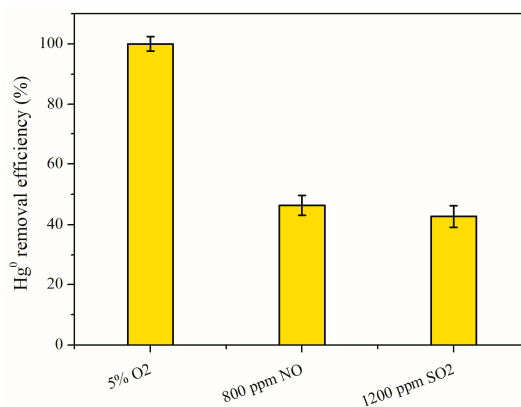


Figure 11. Impact of NO and SO₂ on the mercury conversion of 12Co₃O₄/CNNS.

3.5. Mercury Capture Mechanism

In summary, according to the XPS analysis, Co₃O₄ serves as the main reactive site for elemental mercury capture. The combination of Co₃O₄ with g-C₃N₄ nanosheet increased the catalyst surface area as well as enhancing the redox capability of the catalyst, which is beneficial for the oxidation removal of elemental mercury. Additionally, the production of the Co₃O₄/g-C₃N₄ hybrids reduced the potential energy barrier and boosted the charge transfer mobility, which facilitates elemental mercury removal. Hence, the Hg⁰ removal processes using Co₃O₄/g-C₃N₄ hybrids could be summarized into three stages. (i) The gas-phase Hg⁰ and O₂ adhere on the catalyst exterior to produce adhered mercury (Hg⁰_{ad}) and chemisorbed oxygen (O_{ad}). (ii) The Hg⁰_{ad} is oxidized into Hg²⁺ by the Co³⁺ cations in Co₃O₄ (Hg⁰_{ad} + 2Co³⁺ → Hg²⁺ + 2Co²⁺). The produced Hg²⁺ cations react with O_{ad} or the lattice oxygen (O_{lat}) of Co₃O₄ to generate HgO, which is then captured on the g-C₃N₄ exterior. (iii) The oxygen in the feed gas can refresh the depleted O_{ad} or O_{lat}, and oxidize Co²⁺ into Co³⁺ to rebirth the active phase

Co₃O₄. In addition, since HgO is stable only at temperature below ~300 °C [43], the adsorbed HgO would decompose into elemental mercury again under high-temperature treatment. Therefore, the used Co₃O₄/g-C₃N₄ can be facily regenerated under heating treatment above 300 °C.

4. Conclusions

The pristine g-C₃N₄ nanosheet has a strong attraction towards Hg⁰ adsorption at 120 °C, with a Hg⁰ removal efficiency of ~59.0%. The incorporation of Co₃O₄ with g-C₃N₄ nanosheet could strengthen the mercury capture ability, likely due to the cooperative effect of Co₃O₄ and g-C₃N₄. The loading value of Co₃O₄ could affect the Hg⁰ removal performance. The best performance is displayed by 12Co₃O₄/CNNS, with a mercury conversion of >98% within 90–240 °C. Nitrogen monoxide and sulfur oxide can both reduce the mercury conversion by more than a half because of the competing adsorption and side reactions. This research could deliver useful insights into the application of metal oxide/g-C₃N₄ hybrids for the oxidation removal of elemental mercury.

Author Contributions: Z.Z. performed the experiments and characterized the samples. J.W. conceived the project. D.L. designed the experiments, analyzed the data, and wrote the paper.

Funding: This research was subsidized by the Senior Talent Foundation of Jiangsu University (grant no. 18JDG017) and the National Natural Science Foundation of China (grant no. 21237003).

Conflicts of Interest: The authors declare no conflicts of interest.

References

1. Driscoll, C.T.; Mason, R.P.; Chan, H.M.; Jacob, D.J.; Pirrone, N. Mercury as a global pollutant: Sources, pathways, and effects. *Environ. Sci. Technol.* **2013**, *47*, 4967–4983. [[CrossRef](#)]
2. Schofield, K. Mercury emission control from coal combustion systems: A modified air preheater solution. *Combust. Flame* **2012**, *159*, 1741–1747. [[CrossRef](#)]
3. Xie, J.; Yan, N.; Yang, S.; Qu, Z.; Chen, W.; Zhang, W.; Li, K.; Liu, P.; Jia, J. Synthesis and characterization of nano-sized Mn-TiO₂ catalysts and their application to removal of gaseous elemental mercury. *Res. Chem. Intermed.* **2012**, *38*, 2511–2522. [[CrossRef](#)]
4. Galbreath, K.C.; Zygarlicke, C.J. Mercury transformations in coal combustion flue gas. *Fuel Process. Technol.* **2000**, *65–66*, 289–310. [[CrossRef](#)]
5. Jampaiah, D.; Ippolito, S.J.; Sabri, Y.M.; Tardio, J.; Selvakannan, P.R.; Nafady, A.; Reddy, B.M.; Bhargava, S.K. Ceria-zirconia modified mnox catalysts for gaseous elemental mercury oxidation and adsorption. *Catal. Sci. Technol.* **2016**, *6*, 1792–1803. [[CrossRef](#)]
6. Xu, H.; Jia, J.; Guo, Y.; Qu, Z.; Liao, Y.; Xie, J.; Shangguan, W.; Yan, N. Design of 3D MnO₂/Carbon sphere composite for the catalytic oxidation and adsorption of elemental mercury. *J. Hazard. Mater.* **2018**, *342*, 69–76. [[CrossRef](#)]
7. Sjostrom, S.; Durham, M.; Bustard, C.J.; Martin, C. Activated carbon injection for mercury control: Overview. *Fuel* **2010**, *89*, 1320–1322. [[CrossRef](#)]
8. Luo, G.; Yao, H.; Xu, M.; Cui, X.; Chen, W.; Gupta, R.; Xu, Z. Carbon nanotube-silver composite for mercury capture and analysis. *Energy Fuels* **2010**, *24*, 419–426. [[CrossRef](#)]
9. Xu, W.; Adewuyi, Y.G.; Liu, Y.; Wang, Y. Removal of elemental mercury from flue gas using CuO_x and CeO₂ modified rice straw chars enhanced by ultrasound. *Fuel Process. Technol.* **2018**, *170*, 21–31. [[CrossRef](#)]
10. Xu, H.; Qu, Z.; Zhao, S.; Mei, J.; Quan, F.; Yan, N. Different crystal-forms of one-dimensional MnO₂ nanomaterials for the catalytic oxidation and adsorption of elemental mercury. *J. Hazard. Mater.* **2015**, *299*, 86–93. [[CrossRef](#)]
11. Jampaiah, D.; Chalkidis, A.; Sabri, Y.M.; Edwin, L.H.; Mayes, E.L.H.; Reddy, B.M.; Bhargava, S.K. Low-temperature elemental mercury removal over TiO₂ nanorods-supported MnO_x-FeO_x-CrO_x. *Catal. Today* **2019**, *324*, 174–182. [[CrossRef](#)]
12. Liu, Y.; Wang, Y.; Wang, H.; Wu, Z. Catalytic oxidation of gas-phase mercury over Co/TiO₂ catalysts prepared by sol-gel method. *Catal. Commun.* **2011**, *12*, 1291–1294. [[CrossRef](#)]
13. Jampaiah, D.; Chalkidis, A.; Sabri, Y.M.; Bhargava, M.K. Role of ceria in the design of composite materials for elemental mercury removal. *Chem. Rec.* **2018**, *18*, 1–14. [[CrossRef](#)]

14. Zhao, B.; Liu, X.; Zhou, Z.; Shao, H.; Xu, M. Catalytic oxidation of elemental mercury by Mn-Mo/CNT low temperature. *Chem. Eng. J.* **2016**, *284*, 1233–1241. [[CrossRef](#)]
15. Samanta, S.; Martha, S.; Parida, K. Facile synthesis of Au/g-C₃N₄ nanocomposites: An inorganic/organic hybrid plasmonic photocatalyst with enhanced hydrogen gas evolution under visible-light irradiation. *ChemCatChem* **2014**, *6*, 1453–1462.
16. Xu, J.; Antonietti, M. The performance of nanoparticulate graphitic carbon nitride as an amphiphile. *J. Am. Chem. Soc.* **2017**, *139*, 6026–6029. [[CrossRef](#)]
17. Xun, H.; Zhang, Z.; Yu, A.; Yi, J. Remarkably enhanced hydrogen sensing of highly-ordered SnO₂-decorated TiO₂ nanotubes. *Sens. Actuators B Chem.* **2018**, *273*, 983–990. [[CrossRef](#)]
18. Wu, J.; Sheng, P.; Xu, W.; Zhou, X.; Lu, C.; Ji, Z.; Xu, K.; Zhu, L.; Zhang, X.; Feng, W. Constructing interfacial contact for enhanced photocatalytic activity through BiOIO₃/g-C₃N₄ nanoflake heterostructure. *Catal. Commun.* **2018**, *109*, 55–59. [[CrossRef](#)]
19. Idrees, F.; Dillert, R.; Bahnemann, D.; Butt, F.K.; Tahir, M. In-situ synthesis of Nb₂O₅/g-C₃N₄ heterostructures as highly efficient photocatalysts for molecular H₂ elution under solar illumination. *Catalysts* **2019**, *9*, 169. [[CrossRef](#)]
20. Tahir, M.; Mahmood, N.; Zhang, X.; Mahmood, T.; Butt, F.K.; Aslam, I.; Tanveer, M.; Idrees, F.; Khalid, S.; Shakir, I.; et al. Bifunctional catalysts of Co₃O₄@GCN tubular nanostructured (TNS) hybrids for oxygen and hydrogen evolution reactions. *Nano Res.* **2015**, *8*, 3725–3736. [[CrossRef](#)]
21. Zhu, H.L.; Zheng, Y.Q. Mesoporous Co₃O₄ anchored on the graphitic carbon nitride for enhanced performance supercapacitor. *Electrochim. Acta* **2018**, *265*, 372–378. [[CrossRef](#)]
22. Xiao, J.; Rabeah, J.; Yang, J.; Xie, Y.; Cao, H.; Brückner, A. Fast electron transfer and OH formation: Key features for high activity in visible-light-driven ozonation with C₃N₄ catalyst. *ACS Catal.* **2017**, *7*, 6198–6206. [[CrossRef](#)]
23. Liu, D.J.; Zhang, Z.; Wu, J. Elemental mercury removal by MnO₂ nanoparticle decorated carbon nitride nanosheet. *Energy Fuels* **2019**, *33*, 3089–3097. [[CrossRef](#)]
24. Liu, D.J.; Lu, C.; Wu, J. Gaseous mercury capture by copper-activated nanoporous carbon nitride. *Energy Fuels* **2018**, *32*, 8287–8295. [[CrossRef](#)]
25. Liu, D.J.; Zhou, W.G.; Wu, J. Effect of Ce and La on the activity of CuO/ZSM-5 and MnO_x/ZSM-5 composites for elemental mercury removal at low temperature. *Fuel* **2017**, *194*, 115–122. [[CrossRef](#)]
26. Li, Y.; Liu, Y.; Wang, J.; Uchaker, E.; Zhang, Q.; Sun, S.; Huang, Y.; Li, J.; Cao, G. Titanium alkoxide induced BiOBr-Bi₂WO₆ mesoporous nanosheet composites with much enhanced photocatalytic activity. *J. Mater. Chem. A* **2013**, *1*, 7949–7956. [[CrossRef](#)]
27. Liu, D.J.; Lu, C.; Wu, J. CuO/g-C₃N₄ nanocomposite for elemental mercury capture at low temperature. *J. Nanopart. Res.* **2018**, *20*, 227. [[CrossRef](#)]
28. Hu, H.; Cai, S.; Li, H.; Huang, L.; Shi, L.; Zhang, D. Mechanistic aspects of deNO_x processing over TiO₂ supported Co-Mn oxide catalysts: Structure-activity relationships and in situ DRIFTS analysis. *ACS Catal.* **2015**, *5*, 6069–6077. [[CrossRef](#)]
29. Xiao, J.; Xie, Y.; Nawaz, F.; Wang, Y.; Du, P.; Cao, H. Dramatic coupling of visible light with ozone on honeycomb-like porous g-C₃N₄ towards superior oxidation of water pollutants. *Appl. Catal. B Environ.* **2016**, *183*, 417–425. [[CrossRef](#)]
30. Shen, B.; Yao, Y.; Ma, H.; Liu, T. Ceria modified MnO_x/TiO₂-pillared clays catalysts for the selective catalytic reduction of NO with NH₃ at low temperature. *Chin. J. Catal.* **2011**, *32*, 1803–1811. [[CrossRef](#)]
31. Bing, W.; Chen, Z.; Sun, H.; Shi, P.; Gao, N.; Ren, J.; Qu, X. Visible-light-driven enhanced antibacterial and biofilm elimination activity of graphitic carbon nitride by embedded Ag nanoparticles. *Nano Res.* **2015**, *8*, 1648–1658. [[CrossRef](#)]
32. Dong, F.; Wu, L.; Sun, Y.; Fu, M.; Wu, Z.; Lee, S.C. Efficient synthesis of polymeric g-C₃N₄ layered materials as novel efficient visible light driven photocatalysts. *J. Mater. Chem.* **2011**, *21*, 15171–15174. [[CrossRef](#)]
33. Yuan, B.; Chu, Z.; Li, G.; Jiang, Z.; Hu, T.; Wang, Q.; Wang, C. Water-soluble ribbonlike graphitic carbon nitride (g-C₃N₄): Green synthesis, self-assembly and unique optical properties. *J. Mater. Chem. C* **2014**, *2*, 8212–8215. [[CrossRef](#)]
34. Liu, D.J.; Zhou, W.G.; Wu, J. CeO₂-MnO_x/ZSM-5 sorbents for H₂S removal at high temperature. *Chem. Eng. J.* **2016**, *284*, 862–871. [[CrossRef](#)]

35. Chen, Z.; Sun, P.; Fan, B.; Liu, Q.; Zhang, Z.; Fang, X. Textural and electronic structure engineering of carbon nitride via doping with π -deficient aromatic pyridine ring for improving photocatalytic activity. *Appl. Catal. B Environ.* **2015**, *170–171*, 10–16. [[CrossRef](#)]
36. Vinu, A. Two-dimensional hexagonally-ordered mesoporous carbon nitrides with tunable pore diameter, surface area and nitrogen content. *Adv. Funct. Mater.* **2008**, *18*, 816–827. [[CrossRef](#)]
37. Teng, Z.; Lv, H.; Wang, C.; Xue, H.; Pang, H.; Wang, G. Bandgap engineering of ultrathin graphene-like carbon nitride nanosheets with controllable oxygenous functionalization. *Carbon* **2017**, *113*, 63–75. [[CrossRef](#)]
38. Tang, X.; Gao, F.; Xiang, Y.; Yi, H.; Zhao, S. Low temperature catalytic oxidation of nitric oxide over the Mn-CoO_x catalyst modified by nonthermal plasma. *Catal. Commun.* **2015**, *64*, 12–17. [[CrossRef](#)]
39. Yang, W.; Liu, Y.; Wang, Q.; Pan, J. Removal of elemental mercury from flue gas using wheat straw chars modified by Mn-Ce mixed oxides with ultrasonic-assisted impregnation. *Chem. Eng. J.* **2017**, *326*, 169–181. [[CrossRef](#)]
40. Sasmaz, E.; Kirchofer, A.; Jew, A.D.; Saha, A.; Abram, D.; Jaramillo, T.F.; Wilcox, J. Mercury chemistry on brominated activated carbon. *Fuel* **2012**, *99*, 188–196. [[CrossRef](#)]
41. Hutson, N.D.; Attwood, B.C.; Scheckel, K.G. XAS and XPS characterization of mercury binding on brominated activated carbon. *Environ. Sci. Technol.* **2007**, *41*, 1747–1752. [[CrossRef](#)]
42. Kijlstra, W.S.; Biervliet, M.; Poels, E.K.; Blik, A. Deactivation by SO₂ of MnO_x/Al₂O₃ catalysts used for the selective catalytic reduction of NO with NH₃ at low temperatures. *Appl. Catal. B Environ.* **1998**, *16*, 327–337. [[CrossRef](#)]
43. Yang, S.; Guo, Y.; Yan, N.; Wu, D.; He, H.; Qu, Z.; Jia, J. Elemental mercury capture from flue gas by magnetic Mn-Fe spinel: Effect of chemical heterogeneity. *Ind. Eng. Chem. Res.* **2011**, *50*, 9650–9656. [[CrossRef](#)]



© 2019 by the authors. Licensee MDPI, Basel, Switzerland. This article is an open access article distributed under the terms and conditions of the Creative Commons Attribution (CC BY) license (<http://creativecommons.org/licenses/by/4.0/>).